

## LES ANALYSIS OF A SUPERSONIC AIR INLET EXPERIENCING BUZZ PHENOMENON

Riwan Hammachi, Romain Gojon, Maxime Fiore, Jérémie Gressier and Stéphane Jamme\*

ISAE-SUPAERO, University of Toulouse, France

\*email: stephane.jamme@isae-supaero.fr

### ABSTRACT

This paper investigates the flow in a supersonic mixed compression air intake using numerical simulation. The configuration has been experimentally tested for different back-pressures imposed by a moving plug set at the exit of the internal intake (throttled) or without plug (unthrottled) for which data are available in the literature and to which the simulations can be compared. The unthrottled and three different throttled positions are investigated using large-eddy simulation (LES). The purpose of the study is to analyze the shock structures and their interaction with the boundary layers developing on the surfaces of the air intake for these different cases. Also, because the experiments reported potential unsteady positions of the shock structures for large throttling ratios and, more generally, to analyze the unsteady phenomena, the spectral proper orthogonal decomposition (SPOD) algorithm has been used.

### INTRODUCTION

Aerobic propulsion systems require sufficient airflow through the engine to operate at nominal conditions. The design of the air intake then plays a key role in the performance of the propulsion system. This is particularly true in the supersonic flight regime where the incoming flow must be decelerated before entering into the core of the engine. The supersonic flight regime involves compressible phenomena: shock waves and expansions from the ramp compression devices or from the inlet cowl lips. The latter can impact the boundary layers developing on the opposite walls. These shock wave/boundary layer interactions (SBLI), which vary according to the flight conditions, have direct consequences on the performance and operation of the supersonic air inlet (Chen *et al.* (2018)). The strong adverse pressure gradient induced by a shock wave on a boundary layer may indeed cause a separation of this low-speed region and lead to the development of a separation bubble. The mass flow rate is then reduced, which is detrimental to the propulsion system.

One major well-known problem of these configurations is the supersonic inlet buzz (Oswatitsch (1980)) which can be a great threat to air-breathing supersonic vehicles. Usually, it is triggered by an accidental downstream pressure- or thermal-driven flow blockage, which can throw the inlet into the undesirable subcritical mode featuring the expected terminal shock standing upstream of the inlet entrance. Once the buzz occurs, self-excited streamwise normal-shock oscillations are generated along with periodic duct pressure fluctuations. This promotes a sharp drop in captured air mass flow and, as a consequence, an engine thrust penalty. The inlet buzz with intense fluid unsteadiness should thus be avoided as much as possible.

Ensuring the efficiency of supersonic air intakes is still a

challenge today because of the complex unsteady flows that need to be captured in off-design conditions, with large effects of turbulence, shocks and acoustic waves that interact with each other. A possible path to study these flow configurations is the use of high fidelity numerical simulation. The large-eddy simulation (LES) approach can be used since it can cope with the above-mentioned flow features at a high but nowadays affordable computational cost. The objective of the present work is to analyze the flow in a supersonic air intake with different back-pressure levels using LES. Its purpose is to characterize the unsteady features of supersonic air inlets and the underlying mechanisms driving the flow when a back-pressure occurs and triggers the buzz phenomenon.

### CONFIGURATION/NUMERICAL SETUP

The flow configuration selected in the present work follows the experiments from Chen *et al.* (2018). The geometry of the air intake can be seen in Fig. 1. In the experiments, the upstream flow is characterized by a Mach number of  $M = 2.41$  (corresponding to an overspeed mode for this air intake designed for a shock-on-lip Mach number of 2), a total pressure of  $p_0 = 100,900$  Pa, and a total temperature of  $T_0 = 294.1$  K. The Reynolds number, based on the upstream quantities and the height  $h = 47.5$  mm of the final straight portion of the air inlet duct, equals 494,640.

Several cases have been investigated in the experiments. The cases differ in the back-pressure imposed at the exit in order to mimic a blockage due to the presence of a downstream engine. This is achieved by placing a plug at the exit of the air inlet duct characterized by a half-top angle of  $15.5^\circ$ . The plug reduces the mass flow and leads to an increase of the back-pressure which modifies the operating point of the air inlet. This procedure allows to investigate different flow regimes of the air inlet, ranging from steady configurations for the mean flow to fully unsteady behaviors featuring the buzz phenomenon. In order to quantify the downstream blockage, a throttling ratio ( $TR$ ) is defined as  $TR = 1 - A_{th,plug}/A_{exit}$ , where  $A_{th,plug}$  is the throat area of the plug and  $A_{exit}$  is the cross-sectional area of the duct exit without plug (see Fig. 1). In the numerical simulations, in addition to the case without plug ( $TR = 0$ ), the latter has been set to different positions to reach throttle ratios of  $TR = 0.35, 0.45$  and  $0.6$ , in order to evaluate how the flow progressively deviates from a steady state. These different cases will be respectively denoted TR0, TR35, TR45 and TR60.

In the present work, the Mach number is kept constant between the different simulations and is the same as the one used in the reference experiments. However, in order to keep a reasonable computational time, the Reynolds number has been

halved to 247,320 in our simulations by changing the viscosity of the flow. The spanwise extent of the computational domain has been set to  $L_z = 3\delta_0$  where  $\delta_0 = 2.4$  mm is an expected estimate of the thickness of the turbulent boundary layer (based on a  $1/7^{\text{th}}$  power law) developing with no pressure gradient on the bottom ramp of the inlet, up to the point where the bow shock generated by the cowl lip would impact the bottom wall in the absence of a boundary layer on the ramp (i.e. using a direct extension of the shock angle, see location IV in Fig. 2). This results in a ratio of  $\delta_0/h = 0.05$  for the thickness of the ramp boundary layer at the first interaction with the cowl-induced shock wave.

All variables of the supersonic incoming flow are specified at the inlet boundary of the domain, while they are all extrapolated at outlets. This is consistent with the supersonic flow condition in either the unthrottled or throttled cases. The ramp and cowl walls of the air inlet are set as adiabatic no-slip walls, while the plug walls are set to adiabatic slip walls when set ( $TR \neq 0$ ). Symmetry is imposed at the upper and lower boundaries, and periodic boundary conditions are used in the spanwise direction (see Fig. 1). The computational grid is refined close to the ramp and cowl walls, as well as in the core region in the vicinity of the entrance of the air intake. At the no-slip walls, the size of the cells have been chosen such that  $\Delta x^+ = 20$ ,  $\Delta y^+ = 1$  and  $\Delta z^+ = 15$ . This results in meshes of around  $160 \times 10^6$  cells.

The compressible LES presented herein are performed using the in-house IC3 flow solver, which solves the spatially filtered compressible Navier-Stokes equations for conserved quantities using a finite volume formulation on unstructured meshes. An explicit third-order Runge-Kutta (RK3) scheme is used for time advancement. 20,000 time steps are necessary to resolve one convective time period  $\Delta T = h/u_{\text{in}}$  of the flow,  $u_{\text{in}}$  being the longitudinal velocity at the inlet boundary of the domain. The solver relies on the Vreman subgrid-scale model (Vreman (2004)) to represent the influence of unresolved small-scale fluid motions. It also features a solution-adaptive methodology which combines a low-dissipative centered numerical scheme and a first order upwind scheme in regions of the flow where discontinuities are present. For this purpose, a dilatation-vorticity-pressure gradient (DVPG) shock sensor based on the values of dilatation  $\beta$ , vorticity  $\omega$  and pressure gradient  $\Delta p$ , is used to identify the discontinuities in the flow. In the cells where the ratio  $\text{DVPG} = \frac{\beta}{\omega} \frac{\Delta p}{p}$  exceeds a defined threshold value (set to unity in the present simulations), the first order scheme is applied while in the other cells, the low-dissipative scheme is kept. Fifty-five convective time periods  $h/u_{\text{in}}$  have been used to converge the flow field and an additional fifty-five  $\Delta T$  have been simulated to extract the statistical data. The total computational cost of a single simulation represents 2 MCPuH on AMD ROME processors.

In order to analyze the phenomena occurring in the air intake for the different throttling ratios and in particular the unsteady phenomena that are expected to occur, the spectral proper orthogonal decomposition (SPOD) algorithm is used. The SPOD method relies on discrete Fourier transform (DFT) and proper orthogonal methods to extract the main energetic structures and their characteristic frequency in the flow field. We use in this work the mathematical basis of the SPOD algorithm in its current and more widely used version relying on the Welch formulation, as introduced by Towne *et al.* (2018) and Schmidt & Colonius (2020). This algorithm is applied to two-dimensional ( $x,y$ ) planes stored in time at the mid position in the spanwise direction. We use 4,000 2D-snapshots of the full two-dimensional simulation domain for

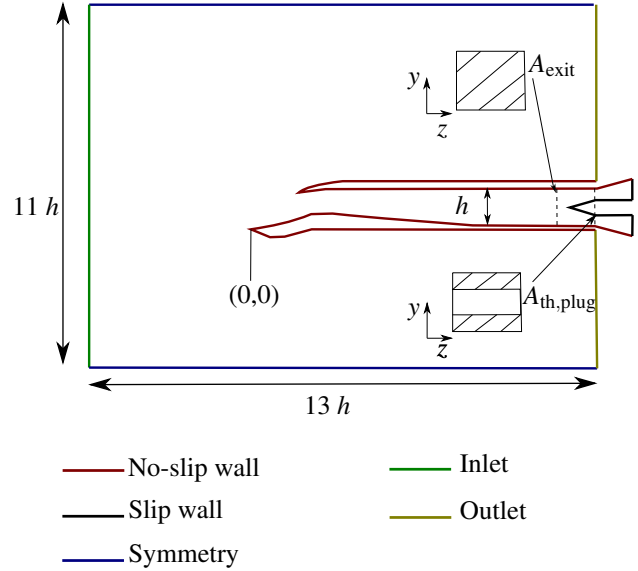


Figure 1: Geometry of the air inlet and associated computational domain in the ( $x,y$ ) plane, featuring a plug at the exit of the inlet duct. The unthrottled case (TR0) does not have any plug.

each LES case with an extraction frequency  $f$  corresponding to  $St = fh/u_{\text{in}} = 70$ . The dataset is partitioned into smaller 50%-overlapping blocks, each of which represents an ensemble realization of the flow. A temporal DFT of each block is then calculated. To reduce spectral leakage, a Hanning window is used to smooth the discontinuities with a hypothetical next period. The frequency resolution corresponds to around  $\Delta St = 0.05$ .

## COMPARISON WITH EXPERIMENTAL DATA

As a validation step for our LES approach, a comparison with experiments is first performed for a steady case where the system of shocks in the air intake is stationary in time. This operating point corresponds to the unthrottled case TR0. Figure 2 shows the corresponding global structure of the flow obtained in the experiments (schlieren) and in the present LES (density gradient). In the experiments, because of installation requirements, the flow data are not available over a box downstream of the cowl lip marked in black in Fig. 2 (a) and the corresponding shock structures have been manually reconstructed *a posteriori* (red lines). The compression of the incoming supersonic flow is achieved across an attached ramp shock (I), followed by an isentropic compression wave fan (II) and a bow shock (III) forming in front of the upper cowl lip. This bow shock impinges on the boundary layer developing on the ramp surface and triggers a flow separation (IV) similar to the one occurring in canonical SBLI. One can notice that the intersection between the ramp shock and the cowl-induced shock occurs inside the inlet entrance. It takes place below the cowl lip because the design Mach number of this air inlet equals 2, which is lower than the freestream Mach number of 2.41 studied in this work. On the upper side of the duct, a subsonic region appears downstream of the bow shock (locally a normal shock wave close to the cowl lip), and full separation from the bottom cowl surface happens due to the deceleration of the flow. Additional shock reflections on the ramp and cowl surfaces then occur further downstream inside the duct. The waves pattern obtained with LES is in good accordance with the experimental schlieren.

A more quantitative comparison with experiments is pre-

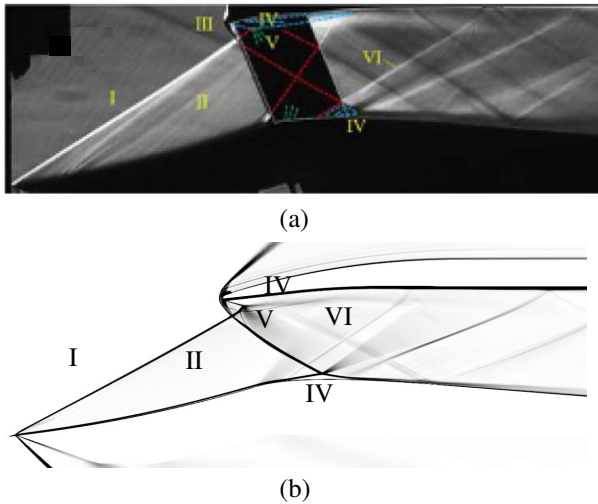


Figure 2: Schlieren image of the unthrottled air inlet (*i.e.* without plug, TR0 case) from Chen *et al.* (2018) (a) ; Contours of the magnitude of the mean density gradients from LES for the same flow configuration (b).

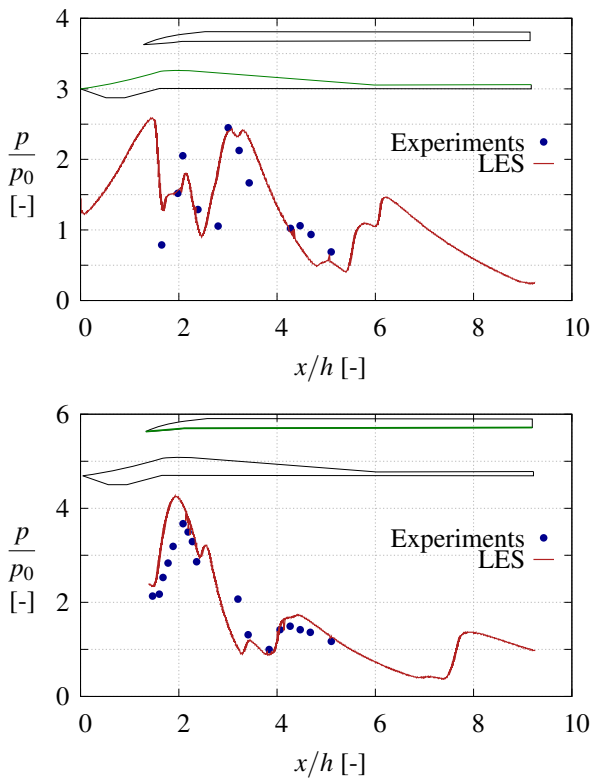


Figure 3: Wall distributions of mean pressure for the TR0 case: ramp side (top) ; cowl side (bottom).

sented in Fig. 3 for the TR0 case where mean pressure distributions along the ramp and the cowl are shown. On the ramp surface (Fig. 3 top), the axial positions of increase/decrease of static pressure obtained with the LES match well the experimental data indicating that the shock structures that cause these pressure variations are well predicted. From the position  $x/h \approx 3$ , an axial shift occurs between the LES and experiments indicating that the shock structures do not match anymore from this position. In terms of amplitude, the decrease

of the pressure is under-predicted at  $x/h \approx 1.6$  but the other measurement locations match well. On the cowl side (Fig. 3 bottom), the positions of the shock structures characterized by the increase/decrease of pressure obtained numerically correspond well to the experiments. In terms of amplitude, the increase of pressure at  $x/h = 1.9$  is slightly over-predicted by the LES. Given the difference in Reynolds number between the present LES and Chen's experiments, a perfect agreement between numerical and experimental data should not be expected. The first SBLIs occurring on the ramp near the inlet section of the intake duct are indeed affected by this Reynolds number discrepancy, which in turn influences the behavior of the subsequent flow. We therefore consider that our LES results can be validated in view of their overall qualitative and quantitative agreement with the reference experiment.

## SPOD ANALYSIS

The focus of the analysis will now be dedicated to the characterization of the unsteadiness level of the flow in the different considered cases (TR0 to TR60). To this purpose, we rely on the SPOD approach previously evoked.

### Unthrottled case TR0

The TR0 case is first studied, because, as stated in the comparison against experiments, this case has a shock cell structure steady in time. The source of unsteadiness is thus expected to be related to turbulence at relatively high frequency compared to buzz phenomena that are expected to induce fluctuations of the flow in the low frequency range. The eigenvalues associated with the two (out of the three) SPOD modes maximizing the fluctuating compressible energy in the domain for the TR0 case are shown in Fig. 4. Each eigenvalue has been normalized by the sum of all eigenvalues for each SPOD mode and over all frequencies (total fluctuating compressible energy in the domain) to provide the relative contribution to this balance of each SPOD mode at each frequency. The analysis showed that the spanwise velocity fluctuations  $u_z^2$  had low eigenvalue magnitudes (low disturbance energy), and that the modes are homogeneous along the span. This is why only the variables  $\rho$ ,  $u_x$ ,  $u_y$ ,  $T$  are considered in the energy disturbance balance. Mode 1 (the most energetic POD mode over all the frequency range denoted SPOD1) exhibits a few main peaks but no large amplitude ratio can be observed between the low frequency range and the other part of the spectrum, which corroborates the steady nature of the shock structures. Moreover, we note that the second most energetic mode SPOD2 has a magnitude two to three times smaller than the mode SPOD1, so that only the mode SPOD1 will be investigated. The spatial structures of density, longitudinal and vertical velocity and temperature fluctuations of the first and second most energetic peaks of SPOD1 at  $St = 0.623$  and  $St = 2.909$  (denoted 1 and 2 in Fig. 4 and sorted from low to large frequency) are shown in Fig. 5. For the first peak corresponding to  $St = 0.623$ , the spatial organization is characterized by large scale structures of density and temperature fluctuations developing inside the inlet duct on the cowl side, as well as more localized longitudinal and vertical velocity structures close to the cowl. An instantaneous snapshot of the actual flow field is shown in Fig. 6. The analysis of the snapshots confirms that the shock cell structures is steady as observed in the experiments. It also shows that the unsteady phenomenon revealed by the SPOD analysis at  $St = 0.631$  can be associated to the shear layer developing at the edge of the flow separation region observed below the cowl. At a higher frequency  $St = 2.909$ , the sec-

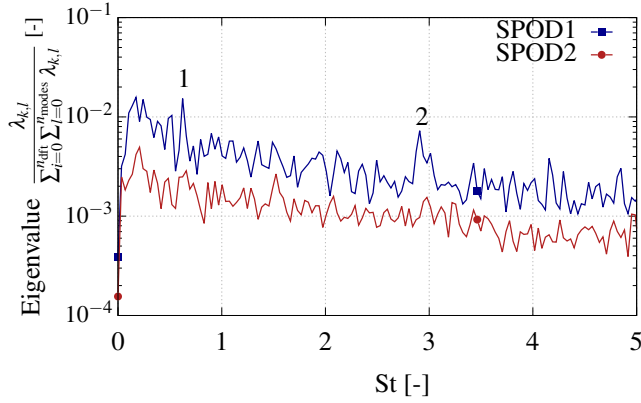


Figure 4: SPOD eigenvalues as a function of frequency (St) for the two most energetic SPOD modes (SPOD1 and SPOD2) based on the fluctuating compressible energy, TR0 case.

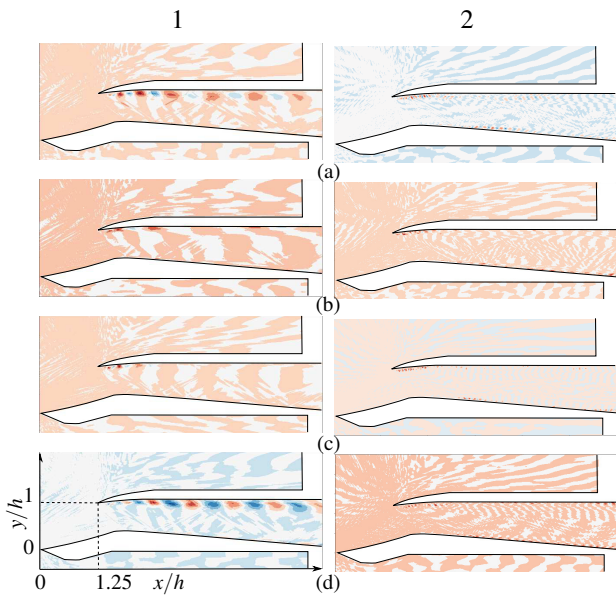


Figure 5: Most energetic spatial structures of density (a), longitudinal (b) vertical (c) velocity and temperature (d) fluctuations related to the peak 1 (left) and 2 (right) of SPOD1, TR0 case. The spatial structures of the modes are scaled between -1 and 1, the energy being held by the corresponding eigenvalue and provided in Fig. 4.

ond peak exhibits structures developing close to the ramp wall around  $x/h = 2.5$ , downstream of the throat. Based on the instantaneous snapshot shown in Fig. 6, these structures can be related to the ramp boundary layer separation due to the impingement of the bow shock developing at the cowl lip. For this operating point, the main unsteadiness is thus related to boundary layer separation at the cowl lip and further downstream on the ramp side due to SBLI. This process related to turbulence spreads the corresponding energy over a broad frequency range, leading to the low amplitude levels observed for the two main SPOD modes in this case.

The unsteadiness related to separation, downstream of the lip on the cowl side and inside the diffuser on the ramp side, can also be observed on the time evolution of the mass flow rate at the throat shown in Fig. 7. The maximum mass flow rate fluctuations represent however no more than 3.8% of the mean mass flow rate for this unthrottled case.

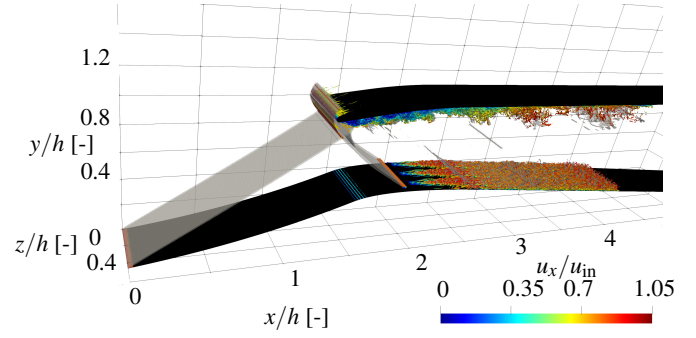


Figure 6: Iso Q-criterion colored by the longitudinal velocity and contours of  $M = 1$  characterizing the shock structures (the simulation domain has been replicated three times in the span-wise direction), TR0 case.

### Throttled cases TR35, TR45 and TR60

We now examine the cases with a non-zero throttling ratio where unsteady effects should be promoted. We present in Fig. 8 instantaneous snapshots of density for the all the cases considered. One can clearly see that, when the back-pressure is increased, the flow inside the duct is strongly affected compared to the TR0 case. If this influence is limited to the downstream part of the duct for TR35, where the waves pattern is similar to the unthrottled case near the entrance of the air inlet, this is no more true for the higher throttling ratios where flow disturbances move further upstream and contaminate the entire duct. The imprint of this behavior on the pressure distribution on the ramp is shown in Fig. 9 where the influence of the back-pressure is striking, with a change in regime for TR60 where the external upstream part of the ramp wall is also contaminated. For TR45 the intersection of the ramp and bow shock is not regular anymore and a Mach stem forms below the cowl lip. Finally, as expected from the pressure distribution, the foot of the bow shock is completely expelled from the duct in the TR60 case, displaying a flow structure characteristic of a strong buzz phenomenon.

The inception of more and more unsteadiness when the throttling ratio increases is also visible in Fig.7. For TR35, the maximum mass flow rate fluctuation represent 11.5% of the mean mass flow rate, this value being greater than the unthrottled TR0 case where the maximum fluctuation reached 3.8%. For the operating point with maximum back pressure (TR60),

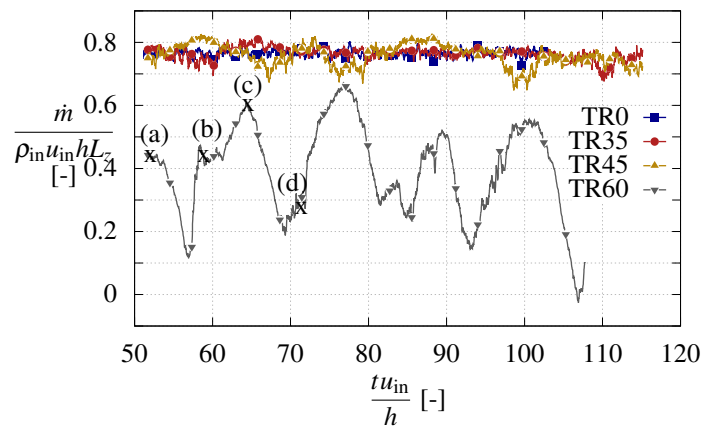


Figure 7: Mass flow rate at the throat as a function of time for the different cases studied. The letters on the TR60 curve mark the instants represented in Fig. 12.

the mass flow rate does not reach the mean value obtained for other operating points. Also, the maximum mass flow rate fluctuation reaches 83.3% of the mean mass flow rate, with an instantaneous mass flow rate that can become very low for some flow events (see for example time  $tu_{in}/h = 58$  in Fig.7).

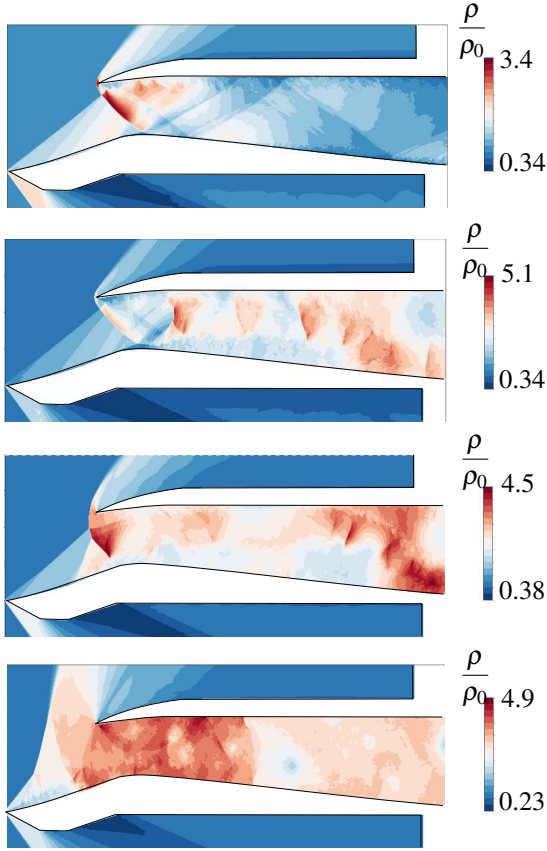


Figure 8: Instantaneous contour of density for the different LES cases. From top to bottom: TR0, TR35, TR45 and TR60.

The SPOD analysis of the throttled cases reveals that a large part of the energy disturbance is held at low frequency, in contrast with what has been observed for the TR0 case. This is illustrated in Fig. 10 which displays the eigenvalues associated with the two (out of the three) SPOD modes maximizing the fluctuating compressible energy in the domain for the TR60 case (to be contrasted with its TR0 counterpart in Fig. 4). In particular, the mode SPOD1 at the frequency  $St = 0.05$  holds 38.4% of the total energy disturbance for TR60 (25.8% for TR35) while the dominant peaks of SPOD1 in the TR0 case did not exceed 2%. Thus, for the throttled cases, the main source of unsteadiness does not correspond to the same mechanism as in the TR0 case.

The mechanisms responsible for this unsteady behavior of the flow can be identified by looking at the spatial structure of the corresponding energetic low-frequency SPOD modes. This can be done for all the throttled cases, but for sake of conciseness, we present herein only the TR60 case that corresponds to the most intense one. Fig. 11 displays the spatial structures of density, longitudinal and vertical velocity and temperature fluctuations of the most energetic peak of mode SPOD1 at  $St = 0.05$ . These spatial structures show that the main mechanisms underlying the activity of the flow at this low frequency are mostly taking place above the external ramp, close to the ramp wall and within a zone delimited by an en-

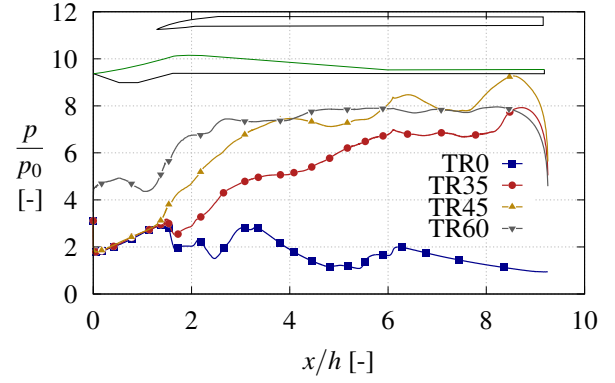


Figure 9: Wall distributions of mean pressure on the ramp side of the duct for the different LES cases.

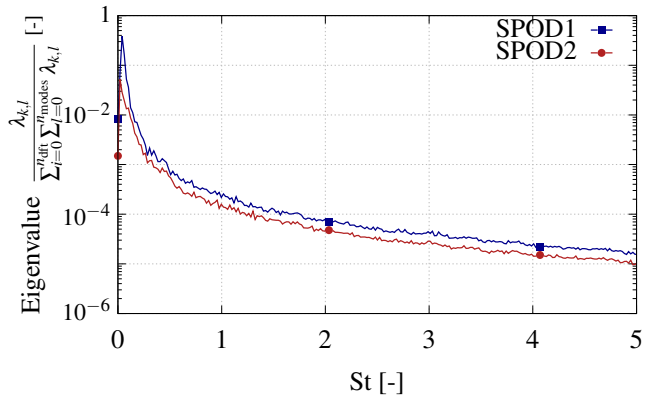


Figure 10: SPOD eigenvalues as a function of frequency ( $St$ ) for the two most energetic SPOD modes (SPOD1 and SPOD2) based on the fluctuating compressible energy, TR60 case.

velope of angles comprised between  $41$  and  $111^\circ$  with respect to the  $x$  axis and centered at the nose of the ramp. Some spots are also visible on the vertical velocity fluctuations inside the duct of the air intake. This information can be correlated with a global oscillation of the flow during which the instability of the ramp-side flow separation plays the dominant role. To that purpose, instantaneous snapshots of the actual flow field describing a period of the phenomenon are shown in Fig. 12, based on isosurfaces of  $Q$ -criterion colored by the longitudinal velocity. The cycle presented in this figure starts at an instant (a) when the ramp-side flow is massively separated due to the strong adverse pressure introduced by the presence of the plug, with the corresponding separation shock at the ramp tip inclined at an angle close to the higher limit of the previously identified envelope on SPOD1 mode. This huge separation leads to a serious blockage of the duct entrance that results in a significant reduction of the inlet mass flow rate in comparison with smaller TR cases (see Fig. 7). The separation bubble first expands and then retracts between instants (a) and (b) so that the minimum mass flow is found between these two snapshots. The bubble subsequently breaks down into a large-scale clockwise-rotating structure that is advected into the diffuser (c), explaining the activity observed on the vertical velocity structure of SPOD1 mode inside the duct, see Fig. 11 (c). Afterwards, the shrunk separation region on the ramp starts to increase again (c), and the inclination of the ramp separation shock wave is at its lower limit of the angle envelope (Note

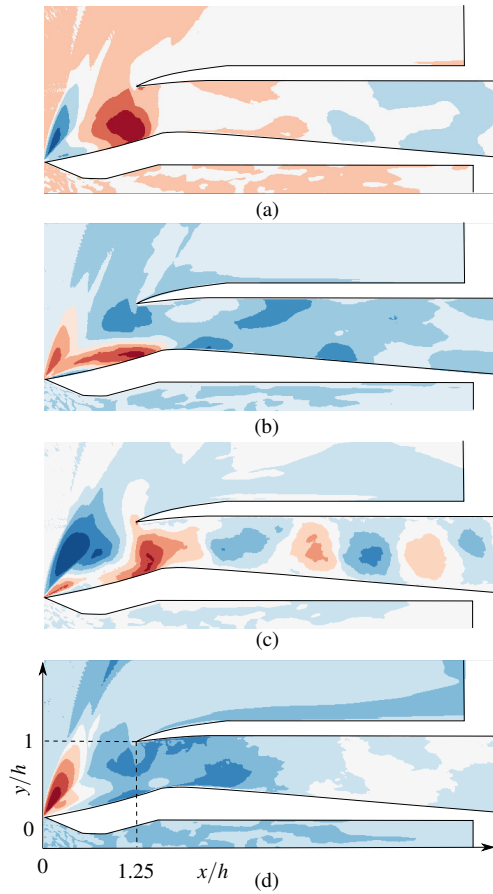


Figure 11: Most energetic spatial structures of density (a), longitudinal (b) vertical (c) velocity and temperature (d) fluctuations related to the dominant peak of SPOD1 ( $St = 0.05$ ), TR60 case.

also that the maximum mass flow rate is obtained close to instant (c) when the separated region on the ramp is small). This process keeps on going (d) and the progressive increase of the extent of the separation region gradually provokes a steepening of the separation shock wave and a return to the beginning of the cycle. This oscillating behavior of the flow operating in the undesirable sub-critical regime of the intake is typically corresponding to the so-called big buzz phenomenon which is here occurring at a frequency around 900 Hz ( $St = 0.076$ ), close to the resolution of our SPOD analysis given the current total duration of our LES simulation.

## ACKNOWLEDGEMENTS

This research was supported by the French Ministry of Defense through the financial support of the DGA (grant #2019-650068004707501). This work was performed using resources from GENCI [CCRT-CINES-IDRIS] (Grant 2021-[A0102A07178]) and CALMIP (Project 1425-21A).

## REFERENCES

- Chen, Hao, Tan, Hui Jun, Zhang, Qi Fan & Zhang, Yue 2018 Throttling process and buzz mechanism of a supersonic inlet at overspeed mode. *AIAA Journal* **55** (5), 1953–1964.
- Oswatitsch, Klaus 1980 Pressure Recovery for Missiles with Reaction Propulsion at High Supersonic Speeds (The Efficiency of Shock Diffusers). In *Contributions to the Development of Gasdynamics*.

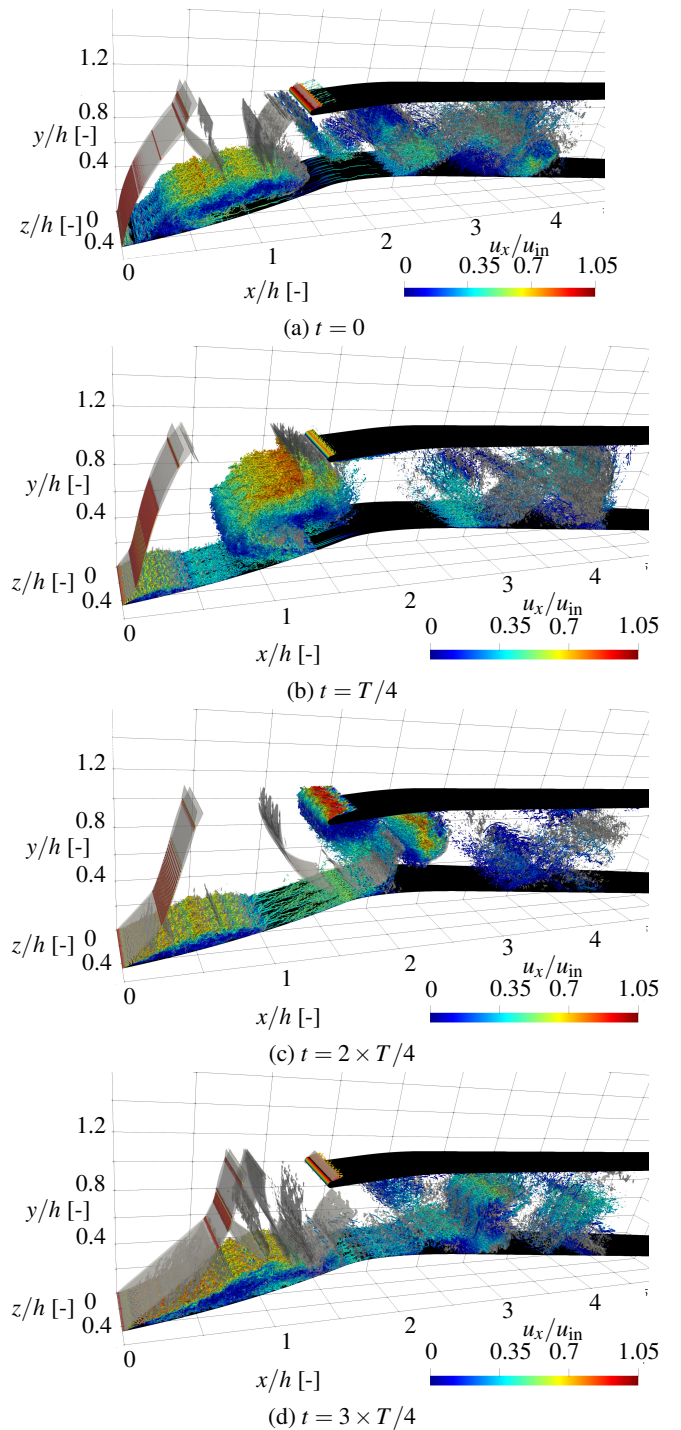


Figure 12: Isosurfaces of Q-criterion colored by the longitudinal velocity at four consecutive instants during a buzz cycle of period  $T$  (the simulation domain has been replicated three times in the spanwise direction), TR60 case.

- Schmidt, O. T. & Colonius, T. 2020 Guide to spectral proper orthogonal decomposition. *AIAA Journal* **55** (12), 4013–4041.
- Towne, A., Schmidt, O. T. & Colonius, T. 2018 Spectral proper orthogonal decomposition and its relationship to dynamic mode decomposition and resolvent analysis. *Journal of Fluid Mechanics* **847** (1), 821–867.
- Vreman, A. W. 2004 An eddy-viscosity subgrid-scale model for turbulent shear flow: Algebraic theory and applications. *Physics of Fluids* **16** (10), 132–144.